

DYNAMICAL MASSES OF YOUNG STARS II: YOUNG TAURUS BINARIES FF TAU, HUBBLE 4 AND HP TAU/G3

AARON C. RIZZUTO¹, TRENT J. DUPUY², ADAM L. KRAUS¹, AND MICHAEL J. IRELAND³

¹Department of Astronomy, The University of Texas at Austin, Austin, TX 78712, USA

²Gemini Observatory, 670 N. Aohoku Place, Hilo, HI 96720, USA

³Research School of Astronomy & Astrophysics, Australian National University, Canberra, ACT 2611, Australia

ABSTRACT

The ages of young associations are often estimated from pre-main-sequence evolutionary models coupled with luminosity and temperature measurements of individual stars. One of the most effective ways to test these models and to age date stars is to combine photometric and spectroscopic measurements with dynamical masses for young binary systems at a range of masses. In this paper, we present orbits of three K/M binary systems in Taurus (FF Tau, Hubble 4 and HP Tau/G3) that have known precise distances from VLBI parallax measurements. For these binary systems, we have measured multi-epoch high-precision astrometry (from Keck-II/NIRC2 and nonredundant aperture-mask interferometry) and relative and system optical photometry (from HST/WFC3-UVIS). We fit the binary system photometry and dynamical masses to a range of pre-main sequence evolutionary tracks and find best-fit model ages of \sim 1-3 Myr, and find that the components of one system, FF Tau AB may be non-coeval. Other similar temperature binary components of the HP Tau/G3 system appear coeval according to the same models, suggesting that the non-coevality is not a model age systematic for components of different mass. Our age estimate for the binary systems differs significantly from the age of the physically associated G-type star HP Tau/G2, which is older (\sim 5 Myr) according to the same models. This discrepancy in age is equivalent to a luminosity under-prediction of 0.1-0.2 dex, or a temperature over-prediction of 100-300 K for K/M-type stars at a given model age. We interpret this as further evidence for a discrepancy in the current generation of pre-main sequence evolutionary tracks for convective stars, as seen in visual and eclipsing binary systems in the 10 Myr Upper Scorpius OB association. **We suggest that the ages of young populations age dated based on M-type star HR diagram position may require upward revision.**

Keywords: stars: young, stars: fundamental parameters, techniques: interferometric, instrumentation: adaptive optics, instrumentation: high angular resolution

1. INTRODUCTION

Age dated stellar populations form the backbone timeline for the study of many different astrophysical processes, including disk evolution and dissipation (e.g., Rieke et al. 2005; Carpenter et al. 2006, 2009; Chen et al. 2011; Rizzuto et al. 2012; Luhman & Mamajek 2012), exoplanet formation and migration (e.g., Kraus & Ireland 2012; Mann et al. 2016a,b; David et al. 2016; Donati et al. 2016) and stellar gyrochronology (e.g., Mamajek & Hillenbrand 2008; Douglas et al. 2016)

In the absence of associated evolved high-mass stars to map the main sequence turn-off, the descent of young low-mass stars onto the main sequence is the most sensitive tool available for dating a young (\lesssim 20 Myr) association. For typical initial conditions, a solar-mass young star contracts to within 20% of its Zero-Age Main Se-

quence (ZAMS) over \sim 30 Myr from an initial radius of more than twice its ZAMS radius - a difference in radius that is relatively easy to detect as an excess luminosity above the main sequence on a traditional HR-diagram. This in-principle sensitivity does not necessarily translate to accuracy. Indeed there are theoretical suggestions (e.g. Baraffe et al. 2012) that there are a range of values for the internal stellar entropy at the conclusion of accretion, as well as a range in initial rotation rates (e.g. Mamajek & Hillenbrand 2008). However, observational evidence suggests that the majority of binary systems appear highly coeval (e.g. Kraus & Hillenbrand 2009a), with only a small minority showing measurable age differences. **Furthermore, it has been shown that in young groups containing stars of all masses, including early-type stars that have begun turning off the main sequence, HR-diagram position**

Table 1. Properties of the three Taurus binary systems.

2MASS	Name	R.A. (J2000)	Decl. (J2000)	SpT	r' (mag)	K (mag)	π (mas)
J04352089+2254242	FF Tau	04 35 20.90	+22 54 24.3	K8	13.1	8.59	6.20 ± 0.03
J04184703+2820073	Hubble 4	04 18 47.04	+28 20 07.3	K8.5	12.0	7.29	7.686 ± 0.032
J04355349+2254089	Hp Tau/G3	04 35 53.50	+22 54 09.0	M0.6	...	8.80	6.20 ± 0.03
J04355415+2254134	Hp Tau/G2	04 35 54.15	+22 54 13.6	G2	10.6	7.23	6.20 ± 0.03

NOTE—Spectral types are taken from Herczeg & Hillenbrand (2014), r' and K band magnitudes are taken from APASS (Henden et al. 2012) and 2MASS (Skrutskie et al. 2006) with typical uncertainties of 0.1 and 0.02 mags respectively. System parallaxes are from the VLBI observations of Torres et al. (2007, 2009) for HP Tau/G3 and FF Tau, and from the latest observations of Galli et al., (in press). We also list the properties for the nearby and associated single G0-type Taurus star HP Tau/G2, from which the parallax measurements for FF Tau and HP Tau/G3 are taken.

does not accurately translate to age for convective stars with the current evolutionary models (e.g. Soderblom 2010; Kraus et al. 2015; Jeffries et al. 2017; Feiden 2016).

Multiple star systems have been a key testing ground for pre-main sequence models (Simon et al. 2013; Schaefer et al. 2014; Montet et al. 2015; Schaefer et al. 2016; Nielsen et al. 2016). For the most part, stars in binary systems appear to be the same age, although a significant minority ($\sim 1/3$) of very young ($\lesssim 3$ Myr) systems show significant age discrepancy between their components (e.g. Kraus & Hillenbrand 2009a). Disentangling dispersion in initial conditions from uncertainties in evolutionary models and real age dispersion within a cluster requires additional data beyond temperature and luminosity. The most readily observable quantity is the dynamical mass, which can be observed through the orbits of binary stars (Boden et al. 2012; Dupuy & Liu 2017, e.g.) or resolved line emission measurements of gaseous circumstellar disks (Simon et al. 2000, e.g.).

With the upcoming Gaia parallax measurements for the majority of young (< 20 Myr) G/K/M-type stars in the wider solar neighborhood (200 pc), we have begun obtaining high-angular resolution monitoring of a large sample of young binary systems in star-forming regions and young associations in order to build a calibration sample for the next generation of models with dynamical mass measurements at the level of the expected Gaia parallax uncertainties (Rizzuto et al. 2016). These measurement will also allow interpretation of the Gaia photocenter motion data for these young binaries, which will be contaminated by significant stellar activity (e.g. Mann et al. 2016b),

In this study, we present the orbits of three close binary systems in the Taurus-Auriga star forming region first discovered during the survey of Kraus et al. (2011a), which have parallaxes measured with very long baseline interferometry (VLBI) or are arguably associated with objects that have VLBI parallaxes. In section 2 we de-

scribe the three Taurus binary systems, in sections 3 and 4 we describe the NIRC2 aperture masking observations and orbit fits to the resulting astrometry, and in section 5 and 7 we describe the analysis of the HST photometry and SED fitting to the binary component luminosities and temperatures. In sections 8 we fit evolutionary models to the data, and in section 9 we discuss the performance of the models, and in section 10 we discuss the implications of the results on the age of the Taurus population.

2. THE TAURUS BINARY SYSTEMS

HP Tau/G3 was identified as a Taurus member by Cohen & Kuh (1979) in a group of stars near HP Tau and has an integrated light spectral type of M0.6 (Herczeg & Hillenbrand 2015). HP Tau/G3 was observed to be a visual binary with contrast of $\Delta K = 1.5 \pm 0.1$ mag during the Keck non-redundant aperture masking survey of Kraus et al. (2011a). It is associated and likely bound to HP Tau/G2, which has a VLBI parallax of 6.2 ± 0.3 mas (Torres et al. 2009). HP Tau/G3 was observed by *K2*, the repurposed *Kepler* mission in field 13 (Howell et al. 2014). Inspection of the *K2* light curve rules out any eclipsing stellar companions.

FF Tau was first identified as a Taurus star by Kenyon & Hartmann (1995), and has an integrated light spectral-type of K8 (Herczeg & Hillenbrand 2015). Kraus et al. (2011a) first identified the $\Delta K = 1.04 \pm 0.02$ mag visual companion with non-redundant aperture mask interferometry. FF Tau was also observed by *K2*, ruling out additional eclipsing companions. We also argue that FF Tau belongs to the same physical association of stars as HP Tau, and so has the same parallax as HP Tau/G2.

HP Tau/G2 and HP Tau/G3 likely form a gravitationally bound system, with several other objects associated with this group. Indeed, within

5 arc minutes one can find the Taurus systems HP Tau AB, FF Tau AB, HP Tau/G2 - HP Tau/G3 AB, KPNO Tau 15 and Haro 6-28. All of these systems have Gaia DR2 (Gaia Collaboration et al. 2018) parallaxes within $1-\sigma$ of the VLBI parallax of HP Tau/G2, except for HP Tau. HP Tau, which appears to be in the background with a parallax of 5.65 ± 0.11 mas was resolved with Lunar occultation interferometry to be a binary system with separation of <20 mas (Richichi et al. 2005). The additional error term in Gaia DR2 is 0.46 mas with a significance of $53-\sigma$, accounting for the offset from HP Tau/G2.

These systems comprise $\sim 5\%$ of the stellar mass of the northern part of the Tau-Aur association, but only $\sim 10^{-6}$ of the area. The alignment is therefore unlikely to be by chance, and we take all these objects to be associated. There is also no clear filamentary structure at the location of these systems in CO(1-0) maps of Taurus (Dame et al. 2001), adding weight to the idea that the objects are physically associated and not simply a filament seen in projection.

Hubble 4 was first cataloged as a star thought to be associated with the reflection nebula near the highly extincted Herbig Be star V892 Tau (Hubble 1922), and was given a spectral type of K8.5 by Herczeg & Hillenbrand (2015). Hubble 4 was identified as a visual binary with contrast of $\Delta K = 0.39 \pm 0.01$ mag with Keck non-redundant masking by Kraus et al. (2011a). It is relatively bright in the radio, and was observed with VLBI to have distance of 132.8 ± 0.5 pc (Torres et al. 2007). Hubble 4 has also been extensively monitored with spectroscopy; Crockett et al. (2012) identified a 0.5-1.5 km/s RV variability on a period of ~ 1.55 days that was determined to be spot-driven. The presence of further spectroscopic companions is unlikely given the lack of larger amplitude RV variability. Table 1 lists the basic properties of these three binary systems.

3. KECK NIRC2 OBSERVATIONS AND ANALYSIS

We have monitored the orbital motion of these three binary systems over the past 7 years with the facility imager NIRC2 at the Keck II telescope, using non-redundant aperture masking (NRM) in the natural guide star AO mode. All NIRC2 AO images were taken with the smallest available pixel scale of 9.952 mas (Yelda et al. 2010) and the nine-hole aperture mask and at multiple IR wavelengths. We employed either a two or four point dither pattern.

The aperture masking reduction used here was the same as presented in Rizzuto et al. (2016), utilizing the

complex triple-product, or closure-phase in addition to squared visibilities to remove non-common path errors. A binary system model, consisting of a separation, position angle and contrast, can then be fit to these observables to determine astrometry. A complete explanation of the reduction and closure-phase fitting method is given in the appendix of Kraus et al. (2008). Table 2 lists the details of the observations and the fitted astrometry for the three binary systems.

4. ORBIT FITTING AND DYNAMICAL SYSTEM MASSES

Orbital solutions were fit to the astrometric data for the three systems with a χ^2 minimization over a grid of orbital parameters. For each system, we first generated an initial sample of 10^4 semimajor-axis, eccentricity, and system mass trial values, spanning 0.5-1.5 times the maximum observed orbital separation and 0.1 to $2 M_\odot$ in total system mass. We drew random masses rather than periods because spectral type information places useful constraints on the system masses and reduces the parameter space involved in the search. We then calculated orbital periods for each trial pair of system mass and semimajor-axis using Kepler's law. For each of the 10^4 random samples we then fit the remaining three orientation angles and periastron time using a Levenberg-Marquardt least squares regression. The χ^2 values for the trials were then inspected in the different orbital parameters to ensure no obvious bi-modality in possible orbits was present. For all three systems, the observations spanned the majority of the full orbit and so the orbital solutions were tightly constrained. We then further restrict the range of trial parameters and draw a new random sample for which the process is repeated. The best fit parameters from this second sample are then taken as the starting point for a full fit over all seven orbital parameters using *mpfit*. Combining our orbit solutions and these parallax measurements, we can estimate the dynamical system masses for the three binary systems. The dynamical masses are listed in Table 3. Table 3 lists the best fit orbital parameters for the three systems and Figure 1 displays the orbital solutions.

5. HUBBLE SPACE TELESCOPE OBSERVATIONS

In addition to AO imaging with Keck/NIRC2, we have also obtained single epoch observations of these binary systems with the Hubble Space Telescope (HST) Wide Field Camera 3 (WFC3), in a variety of visible filters spanning wavelengths of 200–1000 nm. Three exposures were taken in each filter, in the C512C subarray, and the standard HST reduction, calibration, and cosmic ray rejection process was applied (Rajan 2010). We then performed simple aperture photometry on the HST drizzle images with a 0.4" radius target aperture and a sky an-

Table 2. Table of sparse aperture masking observations.

Epoch	MJD	Filter	Sep (mas)	P.A. (deg)	Contrast (mag)
FF Tau					
2007-11-23	54427.579	K'	36.1±0.4	356.4±0.5	1.03±0.02
2008-12-21	54821.520	K'	22.6±2.2	342.0±2.0	1.96±0.36
2008-12-23	54823.463	CH ₄ S	20.8±0.3	335.6±0.3	1.28±0.14
2010-11-29	55528.350	CH ₄ S	20.9±0.3	152.0±0.5	1.19±0.06
2012-01-03	55929.475	CH ₄ S	23.5±0.1	116.3±0.1	1.21±0.01
2012-08-12	56151.572	CH ₄ S	25.6±0.2	98.6±0.2	1.19±0.02
2012-12-04	56265.420	CH ₄ S	26.7±0.1	91.6±0.2	1.23±0.01
2013-08-07	56511.629	CH ₄ S	29.6±0.3	77.3±0.5	1.19±0.02
2014-08-13	56882.584	CH ₄ S	34.7±0.4	62.2±0.5	1.19±0.03
2014-12-09	57000.596	CH ₄ S	36.3±0.3	58.0±0.4	1.29±0.02
2015-12-04	57360.235	K'	41.8±0.3	48.4±0.4	1.07±0.02
2015-12-04	57360.530	Jc	41.3±0.3	47.0±0.4	1.13±0.03
HP Tau/G3					
2007-11-23	54427.583	K'	29.3±1.6	91.8±1.4	1.29±0.18
2008-12-21	54821.525	K'	26.6±0.8	130.6±0.8	1.56±0.10
2009-11-20	55155.478	Kc	22.4±0.9	163.1±2.1	1.393±0.166
2010-11-28	55528.352	CH ₄ S	26.8±1.7	216.7±1.7	1.58±0.11
2012-01-03	55929.235	CH ₄ S	35.7±0.2	244.1±0.2	1.60±0.01
2012-08-12	56151.586	CH ₄ S	42.4±0.5	253.3±0.6	1.59±0.04
2013-08-07	56511.626	CH ₄ S	52.5±0.3	264.7±0.2	1.59±0.02
2014-08-13	56882.644	CH ₄ S	61.2±1.0	274.5±0.7	1.76±0.08
2015-12-04	57360.231	K'	67.7±0.4	280.9±0.3	1.60±0.02
2015-12-04	57360.543	Jc	68.7±0.6	281.2±0.5	1.59±0.07
Hubble 4					
2007-11-23	54427.530	K'	28.4±0.1	106.1±0.1	0.40±0.01
2008-12-21	54821.505	K'	17.0±0.6	284.3±2.8	1.16±0.34
2008-12-23	54823.442	CH ₄ S	17.9±0.1	282.1±0.4	0.60±0.04
2008-12-24	54823.237	K'	16.5±0.5	281.6±2.1	0.70±0.14
2009-11-20	55155.493	Kc	40.0±0.1	228.1±0.1	0.44±0.01
2010-11-29	55528.283	K'	54.4±0.1	207.0±0.1	0.36±0.01
2012-01-03	55929.228	CH ₄ S	63.2±0.1	192.5±0.1	0.39±0.01
2012-08-12	56151.542	CH ₄ S	65.4±0.1	185.9±0.1	0.40±0.01
2012-12-02	56263.555	CH ₄ S	66.4±0.3	183.5±0.4	0.35±0.03
2013-08-06	56510.553	CH ₄ S	65.7±0.1	175.7±0.1	0.37±0.01
2014-08-12	56881.643	CH ₄ S	61.9±0.1	163.9±0.1	0.39±0.01
2015-12-04	57360.239	K'	49.7±0.4	145.5±0.5	0.34±0.03
2015-12-04	57360.263	K'	49.5±0.2	144.6±0.1	0.39±0.01
2015-12-04	57360.525	Jc	50.2±0.2	145.2±0.4	0.49±0.03
2015-12-04	57360.329	Z	49.0±0.6	143.7±0.9	0.52±0.07
2016-11-08	57700.495	CH ₄ S	35.08±0.08	121.24±0.16	0.376±0.007

Table 3. Orbital fits for FF Tau, HP Tau/G3, and Hubble 4.

Name	T_0 (MJD)	P (days)	a (mas)	e	Ω (deg)	ω (deg)	i (deg)	M_{tot} (M_\odot)	χ^2_r
FF Tau	$55168.6^{+5.7}_{-5.6}$	$5393.5^{+66.8}_{-63.5}$	$38.85^{+0.49}_{-0.47}$	$0.634^{+0.004}_{-0.004}$	$176.8^{+0.4}_{-0.4}$	$305.2^{+0.3}_{-0.3}$	$124.9^{+0.5}_{-0.5}$	1.129 ± 0.027	3.2
HP Tau/G3	$54804.1^{+28.0}_{-26.5}$	$9984.4^{+493.7}_{-435.6}$	$56.35^{+0.94}_{-0.76}$	$0.521^{+0.009}_{-0.008}$	$292.5^{+1.5}_{-1.7}$	$200.8^{+5.0}_{-4.7}$	$45.7^{+1.2}_{-1.3}$	1.005 ± 0.053	3.4
Hubble 4	$54703.7^{+0.7}_{-0.7}$	$3394.2^{+2.7}_{-2.7}$	$41.75^{+0.07}_{-0.08}$	$0.681^{+0.001}_{-0.001}$	$66.1^{+0.7}_{-0.8}$	$68.9^{+0.7}_{-0.7}$	$158.7^{+0.4}_{-0.4}$	1.855 ± 0.025	4.4

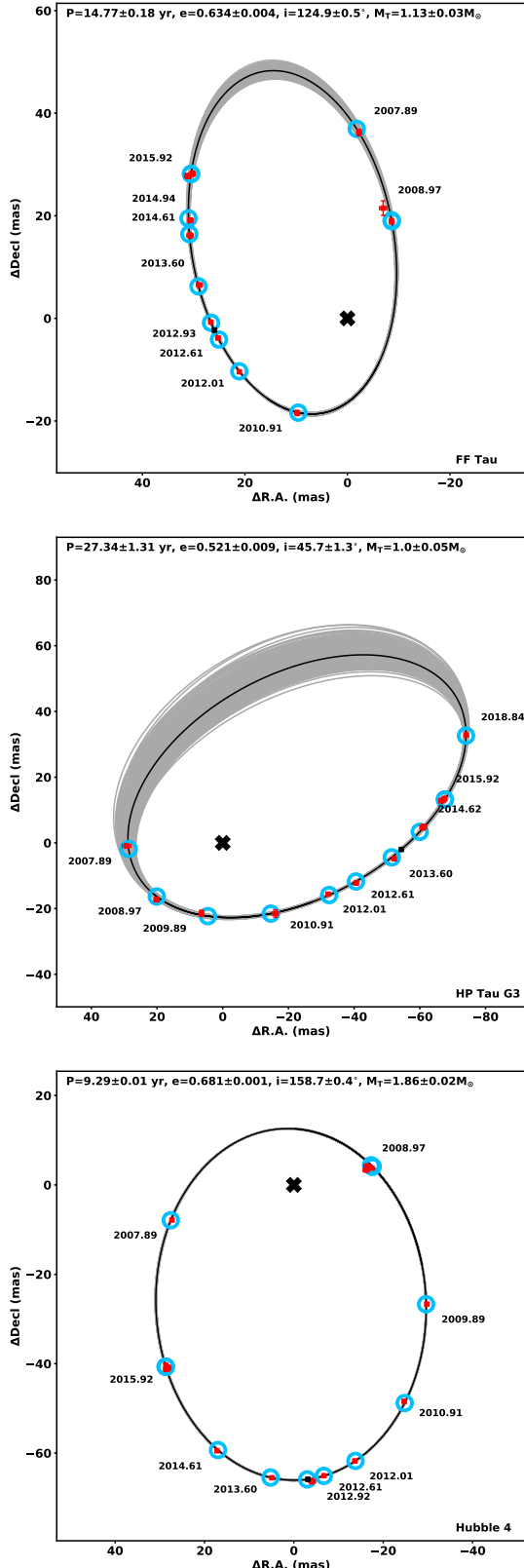


Figure 1. Orbital solution for FF Tau, HP Tau/G3 and Hubble 4. The black curve is the best fit orbit, and the grey curves are 500 random orbits sampled from the fit posteriors. Red squares and blue circles indicate the observed astrometry and model predictions respectively, and the black square indicates the orbital position of the secondary at the time of observation with HST.

nulus of 4–6'', and applied the standard WFC3 zero-point calibration to produce unresolved magnitudes for the systems. Table 4 lists the unresolved system magnitudes in the WFC3 filters, and Table 5 lists unresolved magnitudes from 2MASS and APASS (Skrutskie et al. 2006; Henden et al. 2012).

The epochs of the HST observations are within times spanned by the NRM orbit monitoring observations presented above, and so the relative positions of the binary components are known to ~ 1 mas for each system. The predicted astrometric uncertainties at the HST observation epoch are thus significantly smaller than the HST:WFC3 pixel scale (~ 40 mas), and combined with the stability of the HST point-spread function (PSF) allows decomposition of the highly blended HST/WFC3 images to produce component contrast measurements in the optical bands for the Hubble 4 and HP Tau/G3 systems. FF Tau was found to be too high contrast and too close (sub-WFC3 pixel) at the time of HST observation for decomposition of the images.

Modeled after the work of Garcia et al. (2015) and our previous paper (Rizzuto et al. 2016), we first assembled a library of at least 50 PSFs in each filter in the C512C subarray on the UVIS2 detector from archival data with long exposures. We visually vetted individual PSF references for elongation due to binarity, blends, or nearby cosmic rays within a few pixels of the PSF center. Other contaminants were then handled with sigma clipping in the proceeding fits. Using the Tiny Tim software (Krist et al. 2011) we created PSF models for each WFC3 filter and fit these to the PSF reference library to determine a modified, super-sampled PSF model that most closely fits the library of PSF references.

We then fit the individual images for our binary systems using the new PSF models by sub-pixel shifting and adding the model PSF in each filter to create a model binary system with separation and position angle fixed by the orbit at the epoch of HST observation. Because many of the HST exposures were extremely short (< 1 s) we expected some PSF blur induced by HST's rotational shutter. This is a well documented effect seen in exposures shorter than ~ 5 s (Hartig 2008) and will directly effect the measured component contrasts. We model the shutter blur by applying a 2-dimensional Gaussian blur to the model PSF in the binary fitting procedure, with extent in each axis and angle allowed to vary. Figure 2 displays an example fit to a single WFC3 image. Residuals each image were typically at the $\sim 5\%$ level. Each object had three exposures in each WFC3 filter, and each of these images were fit separately, with different blur parameters and component contrasts. The contrasts and uncertainties were then combined with a mean to determine a final contrast ratio for the systems in each filter. Table 6 lists the contrasts for the Hubble 4

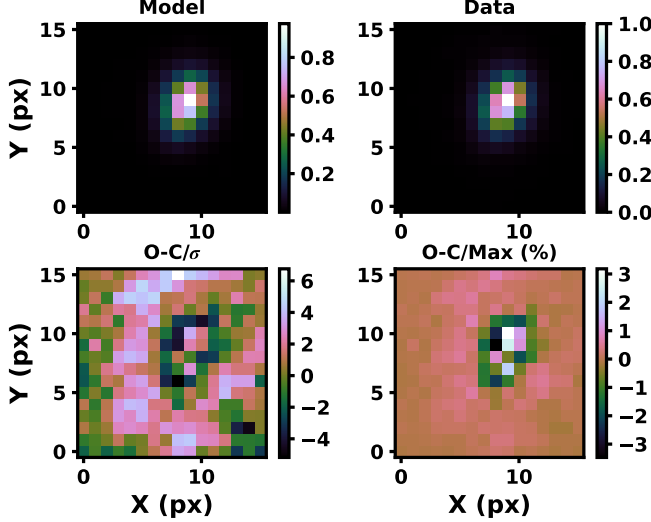


Figure 2. Example two-component PSF fitting to HST:WFC3 data for Hubble 4 in the F625W filter. The model PSF consists of two sources at the separation and position angle predicted by our orbital solutions, and a 2-dimensional Gaussian blur. The resulting residuals are typically at the 1-5% level.

Table 4. HST/WFC3 unresolved photometry.

	FF Tau	HP Tau/G3	Hubble 4
Epoch	2012-10-14	2013-12-01	2012-11-28
F275W	20.38±0.39	20.90±0.59	17.61±0.10
F336W	17.82±0.07	18.85±0.11	15.82±0.03
F390W	16.78±0.03	17.72±0.04	15.16±0.02
F395N	17.41±0.08	18.25±0.12	15.64±0.04
F438W	15.91±0.03	16.88±0.03	14.46±0.02
F475W	14.97±0.02	15.83±0.02	13.63±0.02
F555W	14.02±0.02	14.87±0.02	12.82±0.02
F625W	12.92±0.02	13.66±0.02	11.80±0.02
F656N	12.06±0.03	12.69±0.04	10.84±0.03
F775W	11.66±0.02	12.24±0.02	10.63±0.02
F850LP	10.85±0.02	11.28±0.02	9.76±0.02

and HP Tau/G3 systems

6. WIDE FIELD SPECTROGRAPH OBSERVATIONS

Low-resolution spectra of the three binary systems were obtained with the Wide Field Spectrograph (WiFeS) on the Australian National University 2.3 m telescope (Dopita et al. 2007, 2010). WiFeS is a dual-beam, optical image-slicing spectrograph which provides low to mid resolution spectra over a contiguous 25" by 38" field of view, divided into 1×0.5" spatial pixels. In the red arm, we used the R3000 grating, which provided spectral resolution of $R=3000$ at wavelengths of 5600–9400Å, and in the blue arm we used the B3000 grating which provided spectral resolution of $R=3000$ down to

Table 5. Unresolved catalog photometry.

	FF Tau	HP Tau/G3	Hubble4
J	9.78±0.02	10.04±0.02	8.56±0.02
H	8.93±0.02	9.15±0.02	7.64±0.03
K	8.59±0.02	8.80±0.02	7.29±0.02
B	15.84±0.03	...	14.35±0.08
V	13.87±0.01	...	12.69±0.05
g'	14.86±0.01	...	13.51±0.05
r'	13.07±0.01	...	11.96±0.04
i'	12.06±0.01	...	10.96±0.04

NOTE—J, H and K magnitudes are taken from 2MASS (Skrutskie et al. 2006), and the optical magnitudes are taken from APASS (Henden et al. 2012).

Table 6. HST/WFC3 and NIRC2 magnitude differences for Hubble 4 and HP Tau/G3.

Filter	Hubble 4	HP Tau/G3
F275W	0.78 ±0.11	...
F336W	1.02 ±0.05	...
F390W	0.96 ±0.13	1.89±0.81
F395N	0.88 ±0.10	...
F438W	0.86 ±0.14	3.84±0.72
F475W	1.00 ±0.11	..
F555W	0.99 ±0.25	...
F625W	0.63 ±0.12	3.41±0.33
F656N	0.80 ±0.15	2.20±0.28
F775W	0.51 ±0.26	2.56±0.19
F850LP	0.66 ±0.16	1.60±0.15

Table 7. NIRC2 NIR magnitude differences.

Filter	FF Tau	HP Tau/G3	Hubble 4
z	0.517±0.068
Jc	1.132±0.033	1.576±0.064	0.486±0.032
CH ₄ S	1.219±0.033	1.601±0.028	0.378±0.029
K'	1.052±0.058	1.585±0.106	0.382±0.031
Kc	...	1.393±0.166	0.440±0.010

3200Å. Hubble 4 was observed on December 25 2015, and HP Tau/G3 and FF Tau were observed on 27 December 2015. The observations were taken in poor seeing, and so the data in the blue arm of the spectrograph were of low SNR (<10), as such we only report the red arm spectra here.

The WiFeS data were reduced using the PyWiFeS reduction packages¹(Childress et al. 2014). PyWiFeS transforms the CCD image, consisting of a linear spec-

¹ <http://www.mso.anu.edu.au/pywifes>

trum for each spatial pixel, into a datacube. This includes bias subtraction, flat-fielding, bad pixel and cosmic-ray removal, sky subtraction, wavelength calibration and flux calibration. The data are then interpolated to produce a consistent wavelength scale across each image pixel. We observed a flux calibrator from (?) on each of the two observing nights, which were used for flux calibration of the target spectra. Following this process gives a single cube for each object, with dimensions $25'' \times 38'' \times 3650$ wavelength units. Following this reduction, we then applied the image combining method from (Rizzuto et al. 2015), which fits a 2D-Moffat profile and background flux term to the image at each wavelength slice of the datacube and integrates the full target star flux at each wavelength to produce a linear spectrum. The resulting spectra for our targets had SNR of 40-80 over the wavelength range. Figure 4 displays the WiFeS spectra of the binary systems.

7. TWO COMPONENT SED FITTING

Given the resolved and unresolved photometry for the the binary systems we have obtained from a combination of WFC3 imaging, NIRC2 non-redundant masking observations and the low resolution spectra, it is possible to decompose the combined SED and spectrum of each binary into composite profiles and fit temperatures and luminosities for the components. We use unresolved photometry from WFC3 in the optical and 2MASS in IR. We exclude other catalog photometry to avoid complication due to stellar rotational variability which is common at the 1-10% level in the optical for young (<100 Myr) stars at the expected masses of these binary components (Rizzuto et al. 2017). The WFC3 data was taken in a single telescope visit, and the 2MASS IR data is significantly less contaminated by stellar variability at the longer wavelengths.

We use the BT-Settl atmosphere models in the fitting (Allard et al. 2011), interpolated onto a common wavelength scale in the range of 2000-30000 Å and convolve the models with filter profiles for the WFC3, 2MASS, and NIRC2 filters of interest to produce synthetic fluxes. We then convert the measured unresolved magnitudes from the WFC3 observations to flux measurements using the appropriate zero-points for the aperture size of $0.4''$ used in the aperture photometry (Rajan 2010). We then also apply Gaussian instrumental broadening of $R = 3000$, and some minor rotational broadening of 20 km/s to the component model spectra for comparison to the WiFeS spectra.

We fit a six component model to the resolved and unresolved photometry, consisting of two model temperatures, a radius ratio term, a reddening parameter, and an overall flux scale for both the photometry and the low-resolution

spectrum. For the reddening, we interpolate the Savage & Mathis (1979) reddening law to each filter and apply it to the model photometry and component model spectra. We initially try a small grid of primary and secondary temperatures with starting points chosen based on the integrated light spectral-types and IR flux ratios, and then take the best grid-point as starting parameters for a Levenberg-Marquardt least squares regression. We deliberately exclude any photometry blueward of the F555W filter, as the shorter wavelength filters are typically poorly fit by models for young stars. We also apply a 3σ -clip to reject any photometry that is poorly fit by the models, this resulted in rejection of the F555W unresolved photometry for Hubble 4. We were unable to produce a two component model that fit both the spectrum and the photometry for the Hubble 4 system. While the photometry is able to the fit with two components of temperature $T_{\text{eff}} > 4100$ K, the WiFeS spectrum shows the characteristic TiO regions of a much lower temperature primary. We discuss this further below. Figure 3 shows the final SED fits to the data for the three binary systems, including both the primary and the secondary component contributions to the total flux at each wavelength. **We then determine the component luminosities by integrating the model atmosphere fluxes at the best-fit temperatures according to the flux-scale and ratio terms, and scaling by distance.** Table 8 lists the best-fit temperatures, luminosities, and corresponding radii for HP Tau/G3 and FF Tau.

Following the SED fitting, we then fit the component temperatures and luminosities to evolutionary tracks from the BHAC models (Baraffe et al. 2015) to determine component ages and masses to compare to the total system masses from derived from the orbits. Figure 5 shows the HR-diagram positions of the components of the three binary systems in relation to the 1-10 Myr BHAC isochrones and the corresponding total system masses compared to the dynamical masses. All three systems appear to be younger than ~ 3 Myr. The components of FF Tau also appear to be non-coeval at the $\sim 2\sigma$ level, with the secondary being younger than the primary by ~ 2 Myr. Figure 6 shows the comparison of the dynamical system masses to the model-derived total system masses. There is general agreement between the models and the mass measurements for all three systems, though the comparison is not highly deterministic. For all three models, the total system mass of HP Tau/G3 derived from the models is $\sim 1\sigma$ offset from the empirical values and the other two systems are in closer agreement. The SED fit temperature and luminosity uncertainties dominate the error budget, mainly due to the lack of precision resolved photometry in the optical.

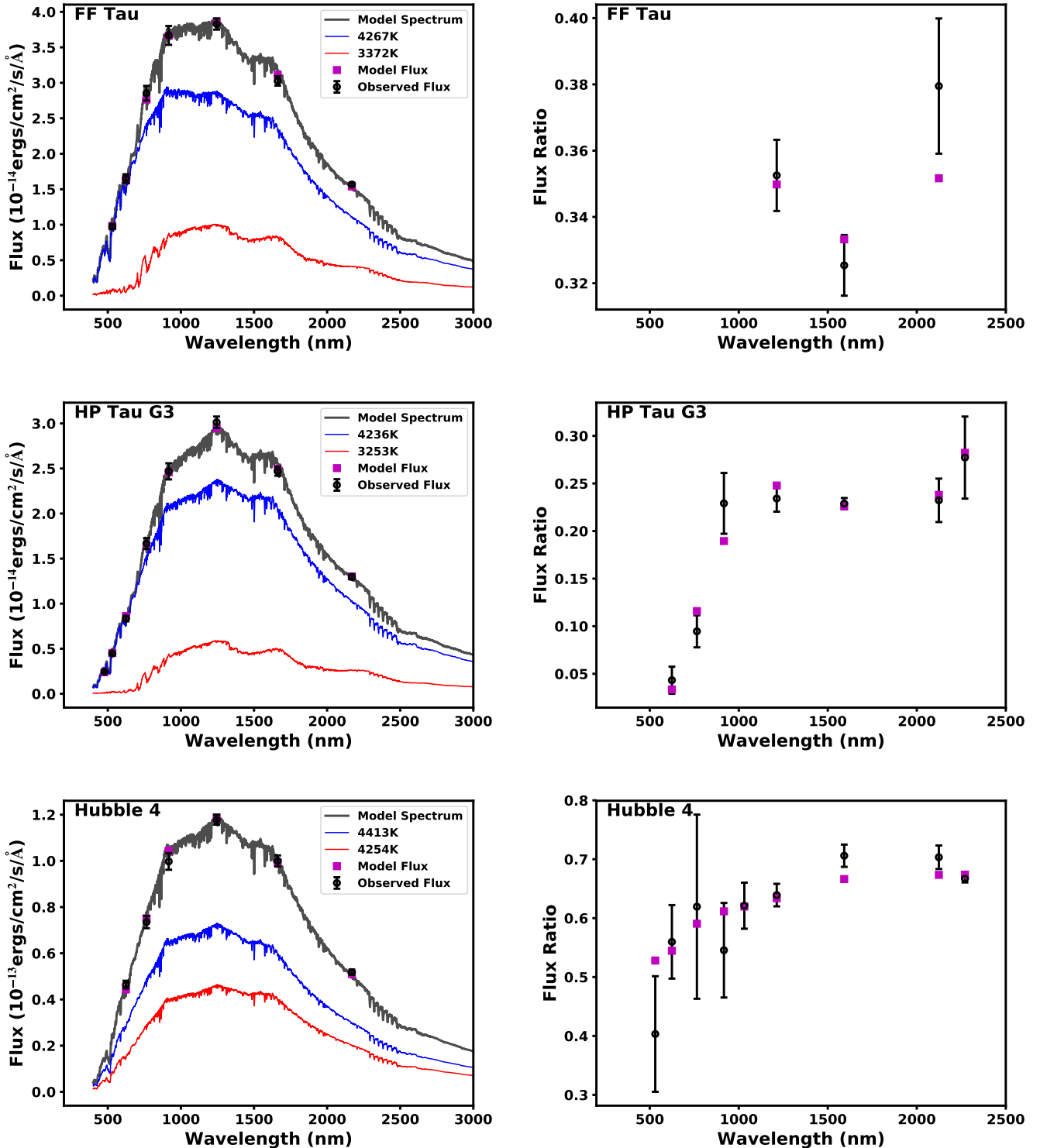


Figure 3. Two component SED fits to the unresolved (*left*) and resolved (*right*) photometry for the three Taurus binaries in our orbit monitoring program. In the unresolved panels, the blue/red atmosphere profiles are the primary and secondary BT-Settl model atmospheres respectively, and the black profile is the combined model spectra. In all panels, black points with error bars are the measurements, and the purple squares are the forward-modeled photometry computed by integrating filter profiles on the model atmospheres and application of the best-fit extinction.

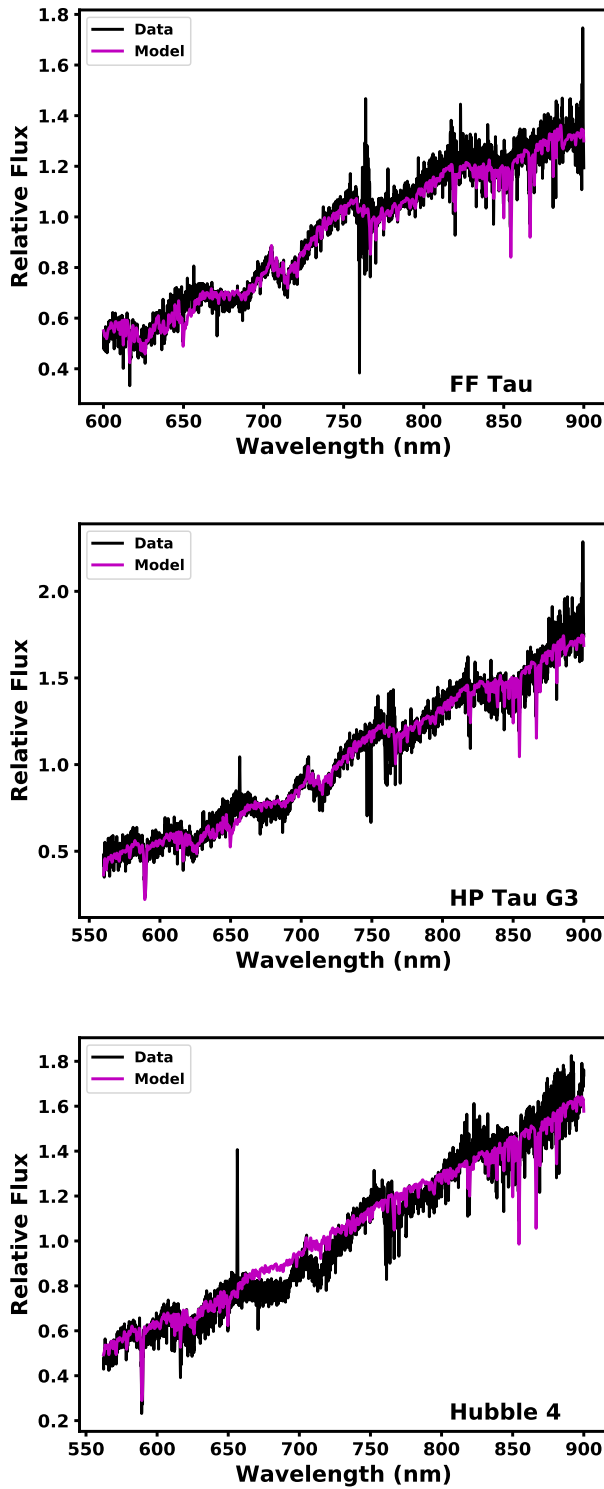


Figure 4. Two component model spectra from the SED fitting compared to unresolved WiFeS spectra. The spectra for FF Tau and HP Tau/G3 match the SED fit profile relatively well, despite expected differences due to the youth of the sources. The unresolved spectrum of Hubble 4 is significantly different to the SED fit component temperature combined spectrum. Given the NIR flux ratios observed in the orbit monitoring data and the component masses from (Galli et al. 2018), we suggest that Hubble 4 may be a hierarchical triple system, with Hubble 4 A being an as yet unresolved binary system.

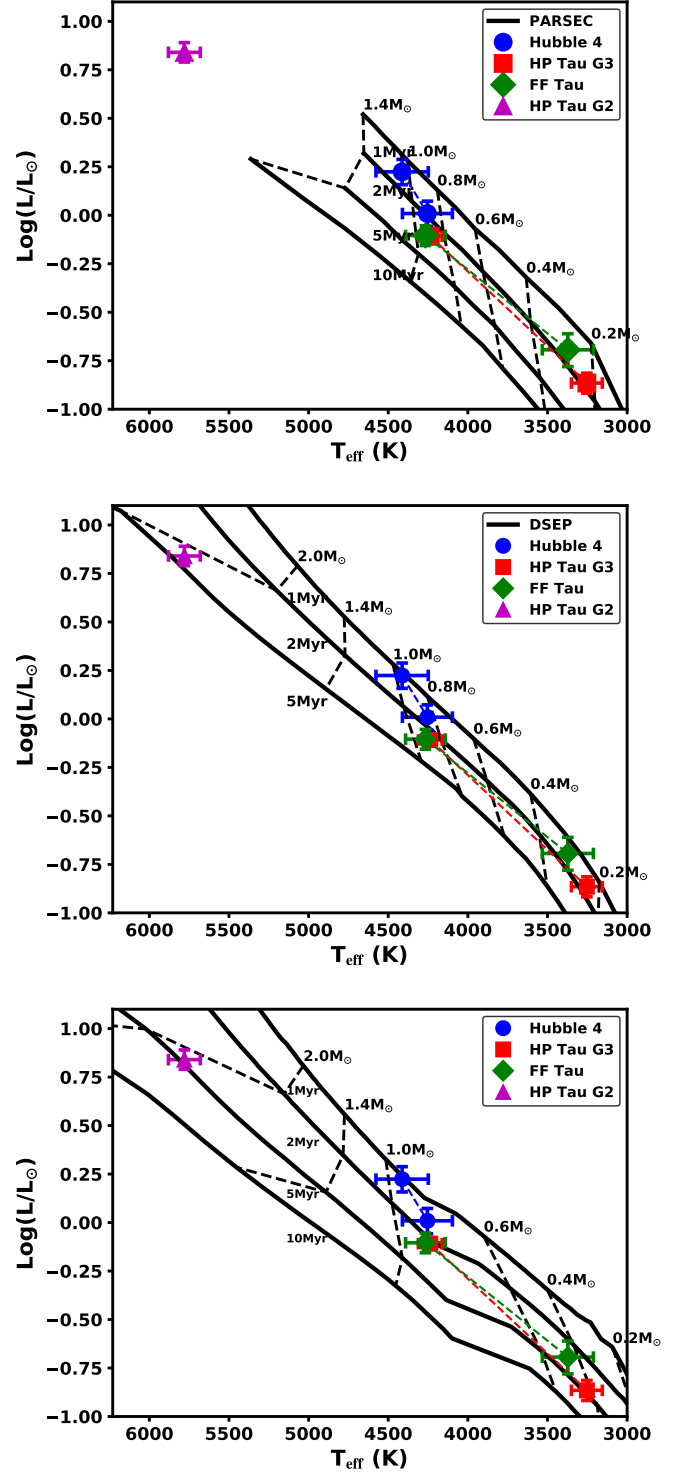


Figure 5. HR-Diagram positions for the components of the three binary systems derived from the SED fitting, and for the three pre-main sequence models. The binary system primary and secondary components are shown as colored points joined by lines. The black grid indicates the isochronal and isomass lines for each of the pre-main sequence models. We also show HP Tau/G2, a single G2-type star at the same distance as HP Tau/G3 and FF Tau, which appears to be significantly older compared to the model grids.

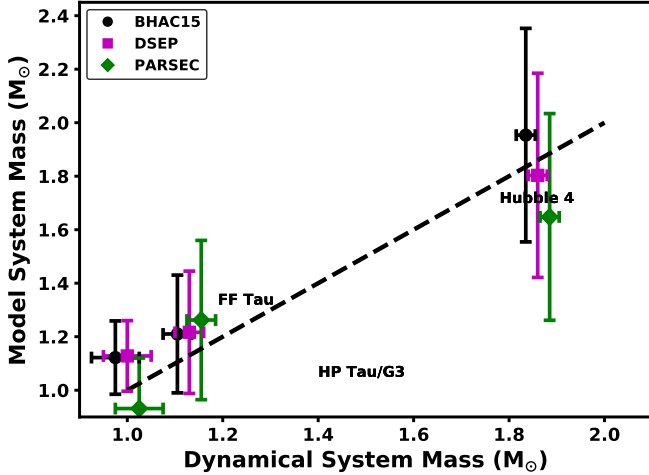


Figure 6. Comparison between the dynamical system masses and masses for the components of the binary systems computed from the SED fit temperatures and luminosities for the Baraffe (Baraffe et al. 2015) (black-circles), DSEP (Dotter et al. 2008) (purple-squares), and Padova PARSEC (Chen et al. 2014) (green-diamonds) isochrones. There is general agreement between the models and the mass measurements, though the comparison is not highly deterministic. The SED fit temperature and luminosity uncertainties dominate the error budget, mainly due to the lack of precision resolved photometry in the optical.

Table 8. BT-Settl SED fit temperatures, luminosities, radii, and corresponding model parameters for the components of the three Taurus binary systems.

	FF Tau	HP Tau/G3	Hubble 4
T _{eff,p}	4266±124	4236±75	4413±164
T _{eff,s}	3372±160	3252±100	4254±156
L _p	0.79±0.10	0.78±0.06	1.67±0.26
L _s	0.20±0.04	0.14±0.02	1.02±0.16
R _p	1.62±0.14	1.64±0.08	2.21±0.24
R _s	1.32±0.20	1.16±0.10	1.86±0.20
E(B-V)	0.66±0.13	0.89±0.05	0.93±0.10
Age _p	3.4±1.3	3.2±0.8	1.5±0.8
Age _s	1.6±0.7	1.9±0.8	1.9±0.8
M _p	0.94±0.14	0.9±0.1	1.06±0.2
M _s	0.27±0.08	0.22±0.05	0.89±0.2
M _{Tot}	1.21±0.22	1.12±0.14	1.95±0.4

8. MODEL ISOCHRONE FITTING

The above model fitting to the SED fit temperatures and luminosities does not simultaneously fit the system mass and photometry to the models. Thus, we fit evolutionary model isochrones to the three binary systems using the Bayesian scheme as presented in Rizzuto et al. (2016), with the addition of a full MCMC parameter-space exploration. This method fits all available information, including photometry, flux ratios, dynamical mass, and parallax to model isochrones. We compared the data to three different models: The Baraffe et al. (2015) BHAC isochrones with BT-Settl atmosphere photometry (Allard et al. 2011), the Padova PARSEC isochrones (Chen et al. 2014), and the Dartmouth Stellar Evolution Program (DSEP) isochrones (Dotter et al. 2008).

For a set of model parameters, we interpolate the model isochrones to the corresponding age and component masses, redden the model photometry (according to Savage & Mathis (1979)) and apply the distance modulus, and then calculate a system mass observable, resolved photometry, and unresolved photometry. These values are then compared to the data and a model likelihood is computed. A full description of the fitting framework can be found in Rizzuto et al. (2016).

We first compare the models to the data on a coarse grid of parameters, with component masses ranging from 0.5 to 1.5 M_{sun} in increments of 0.05 M_{sun}, system age ranging from 1 to 10 Myr in steps of 1 Myr and E(B-V) ranging from 0 to 1.5 mags in steps of 0.1 mags. We identify the grid point which most closely matches the data and use this as a starting point for a MCMC fit using the *emcee* package (Foreman-Mackey et al. 2013). We use 20 walkers for the MCMC fit, initialized randomly around the best fit grid point in a 5-sigma cloud, and sample the posterior PDF 5000 times with each walker, with a 2000 sample burn-in. The output posteriors and chains are then individually inspected to ensure convergence. Table 9 lists the fitted parameters for each system and each model type, with corresponding model component effective temperatures and luminosities.

Table 9. Model fit properties for the Taurus binary system components.

		Age _p (Myr)	Age _s (Myr)	M _p (M _{sun})	M _s (M _{sun})	π (mas)	E(B-V) (mag)	T _{eff,p} (K)	T _{eff,s} (K)	L _p L _{sun}	L _s L _{sun}	χ^2
Hubble 4	BHAC	1.7 ^{+0.1} _{-0.1}	1.7 ^{+0.1} _{-0.1}	1.07 ^{+0.03} _{-0.04}	0.78 ^{+0.03} _{-0.03}	7.69 ^{+0.04} _{-0.04}	0.83 ^{+0.02} _{-0.02}	4415 ⁺²⁶ ₋₂₇	4143 ⁺³¹ ₋₃₀	1.50 ^{+0.05} _{-0.05}	0.90 ^{+0.03} _{-0.03}	1.7
	DSEP	1.5 ^{+0.1} _{-0.1}	1.6 ^{+0.2} _{-0.2}	1.04 ^{+0.05} _{-0.04}	0.81 ^{+0.04} _{-0.04}	7.69 ^{+0.06} _{-0.05}	0.84 ^{+0.03} _{-0.03}	4483 ⁺³⁹ ₋₄₁	4207 ⁺³⁶ ₋₃₉	1.57 ^{+0.08} _{-0.08}	0.93 ^{+0.05} _{-0.05}	3.1
	PARSEC	1.5 ^{+0.1} _{-0.1}	1.5 ^{+0.1} _{-0.1}	1.08 ^{+0.04} _{-0.04}	0.78 ^{+0.04} _{-0.03}	7.68 ^{+0.05} _{-0.05}	0.90 ^{+0.02} _{-0.02}	4561 ⁺³¹ ₋₃₂	4273 ⁺³⁹ ₋₃₁	1.73 ^{+0.08} _{-0.07}	1.04 ^{+0.04} _{-0.04}	2.7

Table 9 continued

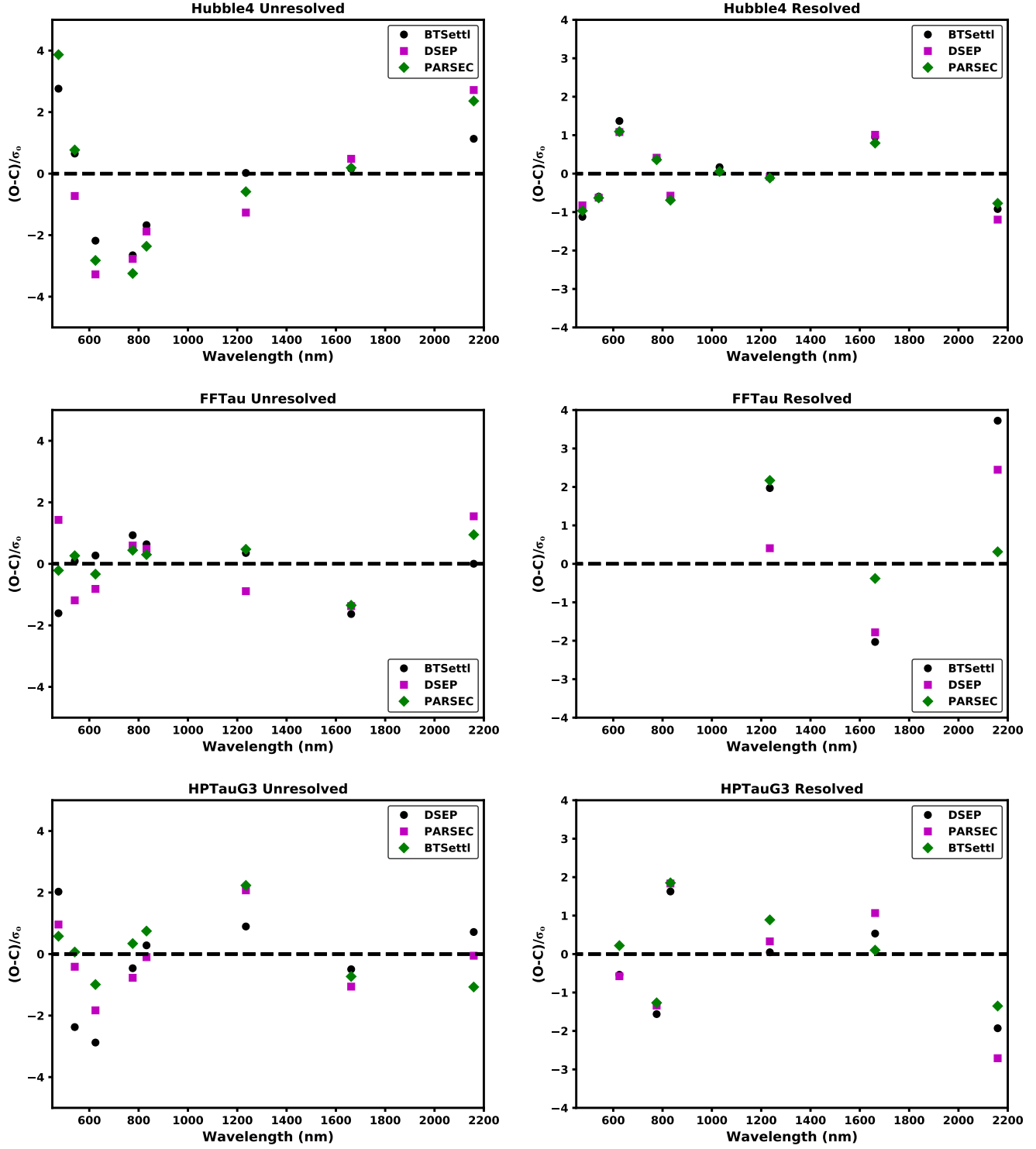


Figure 7. Photometry residuals scaled by measurement uncertainties from the model isochrone fitting for the three Taurus binary systems for the Baraffe (Baraffe et al. 2015) (black-circles), DSEP (Dotter et al. 2008) (purple-squares), and Padova PARSEC (Chen et al. 2014) (green-diamonds) isochrones fits.

Table 9 (*continued*)

		Age _p (Myr)	Age _s (Myr)	M _p (M _⊕)	M _s (M _⊕)	π (mas)	E(B-V) (mag)	T _{eff,p} (K)	T _{eff,s} (K)	L _p L _⊕	L _s L _⊕	χ _r ²
Table 9 (<i>continued</i>)												
		Age _p (Myr)	Age _s (Myr)	M _p (M _⊕)	M _s (M _⊕)	π (mas)	E(B-V) (mag)	T _{eff,p} (K)	T _{eff,s} (K)	L _p L _⊕	L _s L _⊕	χ _r ²
HP Tau/G3	BHAC	3.5 ^{+0.5} -	3.4 ^{+1.0} -	1.02 ^{+0.08} -	0.32 ^{+0.05} -	6.20 ^{+0.04} -	0.98 ^{+0.04} -	4345 ⁺⁷⁴ -	3436 ⁺⁷⁷ -	0.83 ^{+0.05} -	0.139 ^{+0.006} -	0.005
	DSEP	3.2 ^{+0.8} -	3.2 ^{+2.2} -	0.98 ^{+0.15} -	0.33 ^{+0.10} -	6.20 ^{+0.05} -	0.92 ^{+0.08} -	4320 ⁺¹⁶³ -	3407 ⁺¹³⁶ -	0.80 ^{+0.11} -	0.139 ^{+0.008} -	0.008
	PARSEC	2.4 ^{+0.4} -	6.0 ^{+2.3} -	0.84 ^{+0.10} -	0.50 ^{+0.09} -	6.20 ^{+0.04} -	0.93 ^{+0.05} -	4304 ⁺⁸⁷ -	3354 ⁺¹⁰² -	0.83 ^{+0.06} -	0.143 ^{+0.006} -	0.006
FF Tau	BHAC	3.0 ^{+0.5} -	1.4 ^{+1.0} -	0.91 ^{+0.08} -	0.22 ^{+0.13} -	6.21 ^{+0.06} -	0.65 ^{+0.05} -	4244 ⁺⁷⁰ -	3263 ⁺²⁷³ -	0.76 ^{+0.08} -	0.18 ^{+0.02} -	0.01
	DSEP	2.7 ^{+0.2} -	1.2 ^{+0.8} -	0.88 ^{+0.05} -	0.26 ^{+0.07} -	6.20 ^{+0.05} -	0.62 ^{+0.04} -	4214 ⁺⁵⁶ -	3313 ⁺¹²⁵ -	0.74 ^{+0.05} -	0.188 ^{+0.007} -	0.007
	PARSEC	2.4 ^{+0.3} -	1.7 ^{+0.5} -	0.83 ^{+0.07} -	0.30 ^{+0.06} -	6.21 ^{+0.03} -	0.67 ^{+0.03} -	4291 ⁺⁶³ -	3197 ⁺⁶⁴ -	0.81 ^{+0.04} -	0.195 ^{+0.005} -	0.004
FF Tau	BHAC	2.55 ^{+0.07} -	2.55 ^{+0.07} -	0.82 ^{+0.01} -	0.35 ^{+0.01} -	6.20 ^{+0.02} -	0.64 ^{+0.01} -	4149 ⁺²⁰ -	3496 ⁺¹⁴ -	0.72 ^{+0.02} -	0.192 ^{+0.004} -	0.004
(Coeval)	DSEP	2.32 ^{+0.07} -	2.32 ^{+0.07} -	0.81 ^{+0.01} -	0.35 ^{+0.01} -	6.20 ^{+0.02} -	0.60 ^{+0.01} -	4148 ⁺¹⁸ -	3462 ⁺¹² -	0.71 ^{+0.02} -	0.191 ^{+0.004} -	0.004
	PARSEC	2.16 ^{+0.06} -	2.16 ^{+0.06} -	0.78 ^{+0.02} -	0.37 ^{+0.01} -	6.21 ^{+0.02} -	0.65 ^{+0.01} -	4239 ⁺²⁰ -	3623 ⁺¹³ -	0.78 ^{+0.02} -	0.196 ^{+0.004} -	0.004

NOTE—The labels BHAC, DSEP and PARSEC in the second column indicate the parameters are fit using the Baraffe et al. (2015), Dartmouth (Dotter et al. 2008) and Padova PARSEC (Chen et al. 2014) models respectively. In all cases the parallax is strongly determined by the measured VLBI parallax measurements. We also list the model predicted temperatures and luminosities that correspond to the component masses and ages.

9. MODEL COMPARISON

The spectral-types for these binary systems were all K7 (Kenyon & Hartmann 1995), and more recently updated spectral types from optical spectra range from K8-M0.5 (Herczeg & Hillenbrand 2014). These spectral-types imply somewhat cooler effective temperatures than what we find in the SED fitting. Veiling from accretion in the optical is unlikely to have introduced a significant spectral slope, as these stars do not have observable disk material. Indeed, Herczeg & Hillenbrand (2015) estimated that the effect of veiling in the optical for these systems was negligible. We expect that the combination of combined light spectra and variable extinction in the Taurus clouds, and the steep age-mass gradient at this point on the pre-main sequence is the likely cause for the small discrepancy between the integrated-light spectral types, the two component SED temperatures, and the isochrone fit temperature. The model masses for these systems are roughly proportional to the estimated extinction parameters, i.e., the lower mass primaries have smaller values of extinction, which is expected given the integrated light spectral-types.

We also compared the best fit two component model spectrum for each binary system to the unresolved WiFeS spectra. The WiFeS spectra and model SED fit spectra are shown in Figure 4. The spectra for FF Tau and HP Tau/G3 both qualitatively match the model SED fit two

component spectra in the 5600-9000Å wavelength range, indicating the the temperatures and reddening terms we infer from the resolved and unresolved photometry are reliable. The observed spectrum for Hubble 4 is significantly different from the SED model. The TIO bands present in the WiFeS spectrum would indicate a much colder temperature for the components than what we infer from the unresolved photometry and magnitude differences. We note that the WiFeS spectrum implies a combined light spectral type of K7-M0, which is consistent with the temperature estimate of 3900 K from Herczeg & Hillenbrand (2015). It is difficult to reconcile the spectral-type from the optical spectra with the dynamical system mass of 1.856 ± 0.025 measured from the visual orbit, and the NIR primary-secondary flux ratio of ~ 0.65 . Indeed Galli et al. (2018) measured the component masses of the Hubble 4 system using Very Long Baseline Interferometry (VLBI), in combination with the orbit presented in this paper, and found the components to be 1.234 ± 0.023 M_⊕ and 0.730 ± 0.020 M_⊕ respectively. A 1.2 M_⊕ star at < 5 Myr ages is expected to be significantly hotter than 3900 K. We suggest that Hubble 4 may be a hierarchical triple system, with the primary consisting of two stars with temperature closer to ~ 4000 K.

For the two systems with mid-M Type secondaries, HP Tau/G3 and FF Tau, the PARSEC isochrones consistently produce older ages by up

to ~ 2 Myr for the secondary components. This is seen in both the SED fit temperatures dependent on just the photometry (Figure 5), and the full isochrone fit which includes mass information (Table 9). The PARSEC models employ the Atlas models (Castelli & Kurucz 2004) for stars hotter than 4000 K and the PHOENIX BT-Settl model atmospheres (Allard et al. 2011) for stars cooler than 4000 K, to produce the synthetic color-temperature/optical depth relations (Chen et al. 2014). This is then adjusted empirically to better match the colors of M-dwarf cluster members. It is unclear how this calibration to older M-dwarfs might affect our model fitting in the pre-main sequence, in particular if component photometry is produced from different atmosphere models. It is possible that any age difference between components with temperatures on either side of the 4000 K break could be produced by systematics in the PARSEC models.

In both the DSEP and BHAC15 models, the two components of the FF Tau binary system have significantly different ages. The best fit age for the primary component is $\sim 2.7\text{--}3.0$ Myr, and the lower-mass secondary has a best fit age of $\sim 1.2\text{--}1.4$ Myr. While it has been demonstrated that there is a mass-dependent age discrepancy in the pre-main sequence models, in particular with M-type star appearing significantly younger than higher-mass members of the same population (e.g., Pecaut et al. 2012; Kraus et al. 2015; Rizzuto et al. 2016), we do not see the same age difference for the components of HP Tau/G3, which have a similar mass difference and similar temperature components and so we expect this is not explainable as an inconsistency in the models. This rate of non-coevality observed in this small sample of three systems is consistent with larger population estimates in the literature for Taurus (e.g., Kraus & Hillenbrand 2009a) and may be the signature of non-uniform accretion during the gas-rich disk phase of the binary systems life (Baraffe et al. 2009).

We refit the FF Tau data, forcing coevality of the components for all three models. The temperature of the secondary in the coeval case is overestimated by the models by $\sim 250\text{--}375$ K depending on the particular model, corresponding to $2\text{--}3-\sigma$. The primary component temperatures are also underestimated compared to the non-coeval fits though by a much smaller margin (~ 100 K).

The parallaxes and total system masses are well matched by the models for all of the binary systems, with some small disagreement in the photometry, in particular for Hubble 4 and FF Tau. Figure 7 display the residuals for both the unresolved and resolved WFC3

photometry for each binary system and each of the three models. Some structure is present in the unresolved photometry for Hubble 4, with the flux in the F475W filter being over estimated by the models. If the F475W filter is omitted from the analysis consistent model results are obtained, with the remaining photometry well-matched by the models and the residual structure no-longer present. Similarly the unresolved photometry for FF Tau is well fit by the models, however the differential photometry is poorly fit compared to the other systems, despite the lack of optical measurements. This likely reflects the fact that FF Tau B is both the lowest mass and youngest component presented in this study, falling into a region of parameter space not well described by the models (e.g., Dupuy et al. 2016).

FF Tau, HP Tau/G3 and Hubble 4 primaries all show ages ranging from $\sim 1.5\text{--}3.5$ Myr, which is within the expected range for K-type stars in the Taurus clouds. This age is in significant disagreement with the age of the nearby star HP Tau/G2. HP Tau/G2 is at the same distance and is associated with the both FF Tau and HP Tau/G3, and is likely bound to the latter. Kraus et al. (2011b) surveyed HP Tau/G2 with NIRC2 coronagraphy and aperture masking, and did not find a nearby companion.

HP Tau/G2 has a spectral-type estimated from optical spectra of G2 (Herczeg & Hillenbrand 2014), temperature of 5690 K according to their temperature scale and $\log(L/L_\odot) = 0.84 \pm 0.1$ at the measured distance of the system of 161 pc (Torres et al. 2009). The Pecaut & Mamajek (2013) spectra-type to temperature conversion gives an effective temperature of 5870 K which is in agreement with Herczeg & Hillenbrand (2014) within the uncertainties of the temperature scales. These values place HP Tau/G2 at a position on the HR-diagram corresponding to an age closer to ~ 5 Myr, (Figure refmodhrd) which is significantly older than the mean age of the three lower-mass binaries (~ 2.5 Myr).

The stellar membership of the Taurus-Auriga star-forming region is certainly not a coeval population: There are clear regions of ongoing stars formation surrounded by $\sim 1 - 3$ Myr old pre-main sequence stars (Luhman et al. 2009), with a distributed, older disk-free membership identified through spectral youth indicators with ages potentially as old as ~ 20 Myr (Kraus et al. 2017). It is thus possible that comparing two random Taurus stars may result in an age mismatch. This is unlikely to be the case for HP Tau/G2, HP Tau/G3 and FF Tau, which are likely coeval, potentially bound, and not associated with a deep column of gas or dust. The discrepancies in age seen in this coeval test-case are largely mirrored for the wider Taurus population. Kraus

& Hillenbrand (2009a) find that HR-diagram positions of single Taurus stars show a similar mass-age dependence between G and M-type stars.

The age difference between the G-type HP Tau/G2 and the late-type binary systems is most likely the same model discrepancy observed in the somewhat older 10 Myr population in Upper Scorpius (Pecaut et al. 2012; Rizzuto et al. 2016) and attributable to either a luminosity underestimation or temperature overestimation at a particular mass and pre-main sequence age in the model tracks. An underestimation of model luminosities at a given mass and age of 0.1-0.2 dex, or corresponding overestimation in model effective temperature of 100-300 K would account for the age difference between the three Taurus binary systems and HP Tau/G2. This is consistent with the discrepancies observed in the 10 Myr old Upper Scorpius population (Pecaut et al. 2012; Rizzuto et al. 2016), and also the discrepancy seen in LSPM1314, and older field M7 binary system (Dupuy et al. 2016).

10. IMPLICATIONS FOR THE AGE AND STAR FORMATION HISTORY OF TAURUS

There is evidence for a distributed population of slightly older (10-20 Myr) stars surrounding the Taurus clouds (eg., Kraus et al. 2017) that formed in a previous epoch of star formation (much like the Sco-Cen-Ophiuchus complex in the south). The currently highly incomplete sample of this population suggests a very low disk fraction, i.e. most of these objects have undergone disk dissipation. FF Tau, HP Tau/G3, Hubble 4, and HP Tau/G2 do not show evidence of a debris disk in the near-IR or at 10-30 μ m (Andrews & Williams 2005; Luhman et al. 2006; Furlan et al. 2006), though this is not particularly indicative of age. Binary systems undergo disk dissipation on a much shorter timescale than single stars (Kraus et al. 2012), and so the lack of an observable IR excess for the three binary systems is expected **and does not imply membership in the older, distributed population**. In the case of HP Tau/G2, because it is G0-type star, it is not expected to still possess its primordial dust disk. At 10 Myr, only \sim 13% of G-type stars retain a debris disk (Carpenter et al. 2009), and so the lack of a debris disk around HP Tau/G2 is again not indicative of age. The proximity of these systems to the molecular/dust clouds (\sim 1° or \sim 2-3 pc from cloud filament centre), also imply they are likely not part of a distributed older population, but part of the classical Taurus membership.

There is now significant evidence that the current (and previous) generations of pre-main sequence evolutionary models (<20 Myr) under-predict the ages of convective M-type stars in associations of known age in comparison with higher-mass or earlier-type members (Pecaut

et al. 2012; Kraus et al. 2015; Rizzuto et al. 2016; Jeffries et al. 2017). While this discrepancy has previously been seen in older regions (10-20 Myr), we have demonstrated above that the discrepancy extends to a coeval Taurus binary sample that we have monitored. **The classical age for Taurus is 0-2 Myr (Luhman et al. 2009; Kraus & Hillenbrand 2009b)**, and is based on the HR-diagram positions of the majority K/M-type population that make up most of the Taurus census. This then suggests Taurus may be older than the classical age, by up to a factor of two. This may also be the case for other star-forming regions age dated solely on the basis of HR-diagram positions of K/M-types stars using the current evolutionary models.

11. SUMMARY

We have presented precise astrometric orbits and HST WFC3 photometry of three early K/M-type binary systems in the Taurus-Auriga star-forming region. Using the existing radio parallaxes for these systems, we determine system dynamical masses of \sim 1-2% for all three systems, and compare the observational data to evolutionary tracks to determine estimates of component masses, system ages and extinction using a Bayesian fitting technique. In summary, we conclude that:

- The model ages for the components of the FF Tau binary AB system suggest the possibility of non-coevality. Similar temperature components in the HP Tau/G3 system do not show the same age difference, suggesting that this is not a systematic introduced by the models.
- The model isochronal ages derived from fitting to evolutionary models (Baraffe et al. 2015; Chen et al. 2014; Dotter et al. 2008) for the three binary systems give ages in the range \sim 1-3 Myr (excluding the PARSEC ages for the lowest mass components), which differs significantly from the age of the G2-type stars HP Tau/G2, which is physically associated with the binary systems and thus provides a coeval test for the models.
- This discrepancy corresponds to the model luminosities being under-predicted by 0.1-0.2 dex, or the models temperatures being too hot by 100-300 K at a given pre-main sequence age and mass. A consistent discrepancy has been seen previously between G and M-type binaries in the \sim 10 Myr Upper Scorpius population (Pecaut et al. 2012; Rizzuto et al. 2016).

ACKNOWLEDGMENTS

The authors wish to recognize and acknowledge the very significant cultural role and reverence that the summit of Maunakea has always had within the indigenous

Hawaiian community. We are most fortunate to have the opportunity to conduct observations from this moun-

tain.

REFERENCES

- Allard, F., Homeier, D., & Freytag, B. 2011, in Astronomical Society of the Pacific Conference Series, Vol. 448, 16th Cambridge Workshop on Cool Stars, Stellar Systems, and the Sun, ed. C. Johns-Krull, M. K. Browning, & A. A. West, 91
- Andrews, S. M., & Williams, J. P. 2005, ApJ, 631, 1134
- Baraffe, I., Chabrier, G., & Gallardo, J. 2009, ApJ, 702, L27
- Baraffe, I., Homeier, D., Allard, F., & Chabrier, G. 2015, A&A, 577, A42
- Baraffe, I., Vorobyov, E., & Chabrier, G. 2012, ApJ, 756, 118
- Boden, A. F., Torres, G., Duchêne, G., Konopacky, Q., Ghez, A. M., Torres, R. M., & Loinard, L. 2012, ApJ, 747, 17
- Carpenter, J. M., Mamajek, E. E., Hillenbrand, L. A., & Meyer, M. R. 2006, ApJ, 651, L49
- . 2009, ApJ, 705, 1646
- Castelli, F., & Kurucz, R. L. 2004, ArXiv Astrophysics e-prints
- Chen, C. H., Mamajek, E. E., Bitner, M. A., Pecaut, M., Su, K. Y. L., & Weinberger, A. J. 2011, ApJ, 738, 122
- Chen, Y., Girardi, L., Bressan, A., Marigo, P., Barbieri, M., & Kong, X. 2014, MNRAS, 444, 2525
- Childress, M. J., Vogt, F. P. A., Nielsen, J., & Sharp, R. G. 2014, Ap&SS, 349, 617
- Cohen, M., & Kuhi, L. V. 1979, ApJS, 41, 743
- Crockett, C. J., Mahmud, N. I., Prato, L., Johns-Krull, C. M., Jaffe, D. T., Hartigan, P. M., & Beichman, C. A. 2012, ApJ, 761
- Dame, T. M., Hartmann, D., & Thaddeus, P. 2001, ApJ, 547, 792
- David, T. J., et al. 2016, Nature, 534, 658
- Donati, J. F., et al. 2016, Nature, 534, 662
- Dopita, M., Hart, J., McGregor, P., Oates, P., Bloxham, G., & Jones, D. 2007, Ap&SS, 310, 255
- Dopita, M., et al. 2010, Ap&SS, 327, 245
- Dotter, A., Chaboyer, B., Jevremović, D., Kostov, V., Baron, E., & Ferguson, J. W. 2008, ApJS, 178, 89
- Douglas, S. T., Agüeros, M. A., Covey, K. R., Cargile, P. A., Barclay, T., Cody, A., Howell, S. B., & Kopytova, T. 2016, ApJ, 822, 47
- Dupuy, T. J., Forbrich, J., Rizzuto, A., Mann, A. W., Aller, K., Liu, M. C., Kraus, A. L., & Berger, E. 2016, ApJ, 827, 23
- Dupuy, T. J., & Liu, M. C. 2017, ApJS, 231, 15
- Feiden, G. A. 2016, A&A, 593, A99
- Foreman-Mackey, D., Hogg, D. W., Lang, D., & Goodman, J. 2013, PASP, 125, 306
- Furlan, E., et al. 2006, ApJS, 165, 568
- Gaia Collaboration, Brown, A. G. A., Vallenari, A., Prusti, T., de Bruijne, J. H. J., Babusiaux, C., & Bailer-Jones, C. A. L. 2018, ArXiv e-prints
- Galli, P. A. B., et al. 2018, ApJ, 859, 33
- Garcia, E. V., Dupuy, T. J., Allers, K. N., Liu, M. C., & Deacon, N. R. 2015, ApJ, 804, 65
- Hartig, G. F. 2008, WFC3 UVIS Shutter Vibration-Induced Image Blur, Tech. rep.
- Henden, A. A., Levine, S. E., Terrell, D., Smith, T. C., & Welch, D. 2012, Journal of the American Association of Variable Star Observers (JAAVSO), 40, 430
- Herczeg, G. J., & Hillenbrand, L. A. 2014, ApJ, 786, 97
- . 2015, ApJ, 808, 23
- Howell, S. B., et al. 2014, PASP, 126, 398
- Hubble, E. P. 1922, ApJ, 56
- Jeffries, R. D., et al. 2017, MNRAS, 464, 1456
- Kenyon, S. J., & Hartmann, L. 1995, ApJS, 101, 117
- Kraus, A. L., Cody, A. M., Covey, K. R., Rizzuto, A. C., Mann, A. W., & Ireland, M. J. 2015, ApJ, 807, 3
- Kraus, A. L., Herczeg, G. J., Rizzuto, A. C., Mann, A. W., Slesnick, C. L., Carpenter, J. M., Hillenbrand, L. A., & Mamajek, E. E. 2017, ApJ, 838, 150
- Kraus, A. L., & Hillenbrand, L. A. 2009a, ApJ, 704, 531
- . 2009b, ApJ, 704, 531
- Kraus, A. L., & Ireland, M. J. 2012, ApJ, 745, 5
- Kraus, A. L., Ireland, M. J., Hillenbrand, L. A., & Martinache, F. 2012, ApJ, 745, 19
- Kraus, A. L., Ireland, M. J., Martinache, F., & Hillenbrand, L. A. 2011a, ApJ, 731, 8
- . 2011b, ApJ, 731, 8
- Kraus, A. L., Ireland, M. J., Martinache, F., & Lloyd, J. P. 2008, ApJ, 679, 762
- Krist, J. E., Hook, R. N., & Stoehr, F. 2011, in Society of Photo-Optical Instrumentation Engineers (SPIE) Conference Series, Vol. 8127, Society of Photo-Optical Instrumentation Engineers (SPIE) Conference Series
- Luhman, K. L., & Mamajek, E. E. 2012, ApJ, 758, 31
- Luhman, K. L., Mamajek, E. E., Allen, P. R., & Cruz, K. L. 2009, ApJ, 703, 399
- Luhman, K. L., Whitney, B. A., Meade, M. R., Babler, B. L., Indebetouw, R., Bracker, S., & Churchwell, E. B. 2006, ApJ, 647, 1180
- Mamajek, E. E., & Hillenbrand, L. A. 2008, ApJ, 687, 1264
- Mann, A. W., et al. 2016a, ApJ, 818, 46
- . 2016b, AJ, 152, 61
- Montet, B. T., et al. 2015, ApJ, 813, L11
- Nielsen, E. L., et al. 2016, AJ, 152, 175
- Pecaut, M. J., & Mamajek, E. E. 2013, ApJS, 208, 9
- Pecaut, M. J., Mamajek, E. E., & Bubar, E. J. 2012, ApJ, 746, 154
- Rajan, A. e. 2010, WFC3 Data Handbook v. 2.1
- Richichi, A., Percheron, I., & Khristoforova, M. 2005, A&A, 431, 773
- Rieke, G. H., et al. 2005, ApJ, 620, 1010
- Rizzuto, A. C., Ireland, M. J., Dupuy, T. J., & Kraus, A. L. 2016, ApJ, 817, 164
- Rizzuto, A. C., Ireland, M. J., & Kraus, A. L. 2015, MNRAS, 448, 2737
- Rizzuto, A. C., Ireland, M. J., & Zucker, D. B. 2012, MNRAS, 421, L97
- Rizzuto, A. C., Mann, A. W., Vanderburg, A., Kraus, A. L., & Covey, K. R. 2017, AJ, 154, 224
- Savage, B. D., & Mathis, J. S. 1979, ARA&A, 17, 73
- Schaefer, G. H., Prato, L., Simon, M., & Patience, J. 2014, AJ, 147, 157
- Schaefer, G. H., et al. 2016, ArXiv e-prints
- Simon, M., Dutrey, A., & Guilloteau, S. 2000, ApJ, 545, 1034
- Simon, M., Schaefer, G. H., Prato, L., Ruiz-Rodríguez, D., Karnath, N., Franz, O. G., & Wasserman, L. H. 2013, ApJ, 773, 28
- Skrutskie, M. F., et al. 2006, AJ, 131, 1163
- Soderblom, D. R. 2010, ARA&A, 48, 581
- Torres, R. M., Loinard, L., Mioduszewski, A. J., & Rodríguez, L. F. 2007, ApJ, 671, 1813
- . 2009, ApJ, 698, 242
- Yelda, S., Lu, J. R., Ghez, A. M., Clarkson, W., Anderson, J., Do, T., & Matthews, K. 2010, ApJ, 725, 331